Quantifying dorsal closure in three dimensions

Heng Lu[a,†], Adam Sokolow[a,‡], Daniel P. Kiehart[b,*], and Glenn S. Edwards[a,*]
[a]Physics Department and [b]Department of Biology, Duke University, Durham, NC 27708

ABSTRACT **Dorsal closure is an essential stage of *Drosophila* embryogenesis and is a powerful model system for morphogenesis, wound healing, and tissue biomechanics. During closure, two flanks of lateral epidermis close an eye-shaped dorsal opening that is filled with amnioserosa. The two flanks of lateral epidermis are zipped together at each canthus ("corner" of the eye). Actomyosin-rich purse strings are localized at each of the two leading edges of lateral epidermis ("lids" of the eye). Here we report that each purse string indents the dorsal surface at each leading edge. The amnioserosa tissue bulges outward during the early-to-mid stages of closure to form a remarkably smooth, asymmetric dome indicative of an isotropic and uniform surface tension. Internal pressure of the embryo and tissue elastic properties help to shape the dorsal surface.**

Monitoring Editor
Denise Montell
University of California, Santa Barbara

Received: Jun 15, 2016
Revised: Sep 12, 2016
Accepted: Oct 18, 2016

INTRODUCTION

Morphogenesis is a consequence of multiple regulatory and biomechanical processes that contribute to molecular, cellular, and tissue dynamics (Keller *et al.*, 2003). Dorsal closure begins ~10 h after egg laying and takes ~3 h to complete (at room temperature; Kiehart *et al.*, 2000; Harden, 2002; Jacinto *et al.*, 2002b). Figure 1A presents a three-dimensional (3D) schematic of an embryo during early dorsal closure that locates the opening on the dorsal surface. This dorsal opening is filled with amnioserosa, which is a transient tissue and a simple (one-cell-thick) epithelium. At the conclusion of closure, the two flanks of lateral epidermis have converged to close the dorsal opening, providing the embryo with a continuous epithelium. The progression of closure is summarized in Figure 1B and Supplemental Movie S1. Here the cross-sections of (initially) ~200 polygonal amnioserosa cells were outlined by the fluorescence due to green fluorescent protein (GFP)–labeled DE-cadherin, which concentrated predominantly in subapical belts of adherens junctions. Two supracellular, actomyosin-rich purse strings fluoresced due to red fluorescent protein (RFP)–labeled moe-ABD (the F-actin binding domain of moesin).

More than 130 gene products, subject to posttranscriptional, translational, and posttranslational processing, regulate dorsal closure (Harden, 2002; Jacinto *et al.*, 2002b; Franke *et al.*, 2005; Attrill *et al.*, 2016). The leading-edge cells are transcriptionally distinct from the rest of the lateral epidermis (Foe and Alberts, 1983; Harden, 2002). Throughout closure, complex protein redistributions remodel the cytoskeleton and cell–cell and cell–matrix junctions (e.g., Kiehart *et al.*, 2000; Kaltschmidt *et al.*, 2002; Jankovics and Brunner, 2006; David *et al.*, 2010; Mateus and Martinez Arias, 2011). There is no cell division in the amnioserosa and little if any in the lateral epidermis during closure.

The junctions between the amnioserosa and the two leading edges of the lateral epidermis exhibit complex structure and dynamics. The peripheral-most amnioserosa cells extend underneath either leading edge (Narasimha and Brown, 2004; Rodriguez-Diaz *et al.*, 2008). At each canthus, apposing leading edge cells are zipped together into a seam (Jacinto *et al.*, 2000; Lu *et al.*, 2015). At the end of closure, the remaining amnioserosa has moved beneath the seam and undergoes apoptosis (Figure 1B, 125 min; see Figure 1 in Rodriguez-Diaz *et al.*, 2008; Kiehart *et al.*, 2000). Eventually, the actin-rich purse strings disassemble, and after dorsal closure, a continuous epithelium results (Kiehart *et al.*, 2000).

The biomechanics of native dorsal closure comprises a system of four biological processes (Hutson *et al.*, 2003; Peralta *et al.*, 2007). 1) The lateral epidermis resists closure. 2) Each purse string is under tension and promotes closure. 3) The amnioserosa pulls the two leading edges toward the dorsal midline and also promotes closure

This article was published online ahead of print in MBoC in Press (http://www.molbiolcell.org/cgi/doi/10.1091/mbc.E16-06-0400) on October 26, 2016.

Present addresses: †Technical Institute of Physics and Chemistry, CAS, Beijing 100190, China; ‡Army Research Laboratory, Aberdeen Proving Ground, MD 21005.
*Address correspondence to: Daniel P. Kiehart (dkiehart@duke.edu), Glenn S. Edwards (gedwards@phy.duke.edu).

Abbreviations used: α_{AS}, amnioserosa surface tension coefficient; Δa, cross-sectional area of an amnioserosa cell; ΔP, pressure difference across the amnioserosa; κ_{A-P}, principal curvature in the anteroposterior plane; κ_{L-R}, principal curvature in the left-right plane; Ant, anterior; A–P, anteroposterior; AS, amnioserosa; Avg, average; 2D, two-dimensional or two dimensions; 3D, three-dimensional or three dimensions; DE-cadherin, *Drosophila* E-cadherin; GFP, green fluorescent protein; L, left; LE, leading edge; L–R, left-right; moe-ABD, filamentous-actin binding domain of moesin; NA, numerical aperture; Pos, posterior; R, right; R_{A-P}, principal radius of curvature in the anteroposterior plane; RFP, red fluorescent protein; R_{L-R}, principal radius of curvature in the left-right plane.

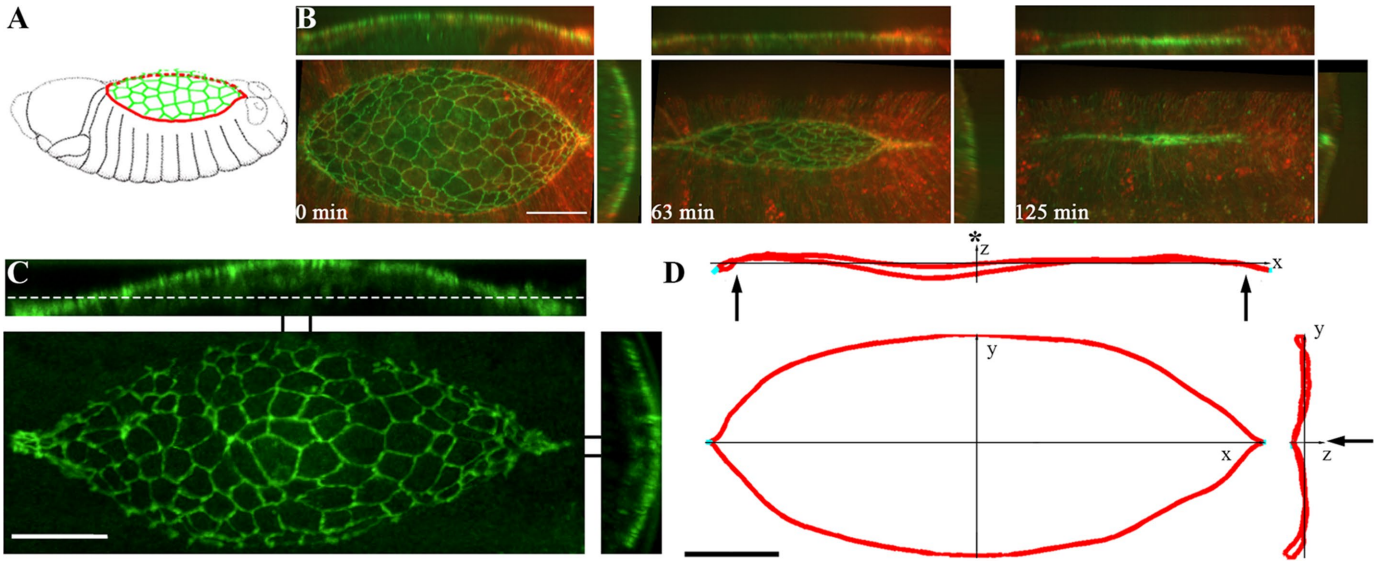

FIGURE 1: Three-dimensional dorsal closure. (A) Schematic diagram of an embryo during an early stage of closure. Red outlines both purse strings and green outlines the amnioserosa cells (which dome above the purse strings). Modified from flybase.org/reports/FBim0000636.html. (B–D) Dorsal (main image), sagittal (top horizontal image), and transverse (right vertical image) views, where pairs of black lines to the right and above the main image indicate the projected range used to produce the transverse and sagittal sections. (B) Three confocal fluorescence images show the progress of closure in an embryo labeled with GFP–DE-cadherin (green) and RFP-moe-ABD (red). The time stamp 0 min corresponds to the first image collected. (C) GFP–DE-cadherin embryo early in closure exhibiting both the dorsal opening and the amnioserosa dome. The white dashed line in the top image was determined by the apical surfaces of the two seams. (D) Purse strings (red indicates leading edges; cyan at the ends indicates seams) from a segmented confocal image of a GFP-moe-ABD embryo during an early stage of closure. Projecting the entire segmented image generated the sagittal and transverse sections. The three arrows indicate large bends near the ends of the purse strings, and the asterisk indicates the location of the maximal dorsal opening. Anterior is to the left. Scale bar, 15 μm (B), 30 μm (C, D).

(Sokolow *et al.*, 2012). 4) During zipping, the two apposing leading edges merge and are incorporated into a seam at each canthus, where contraction of each purse string (on average) occurs as part of the zipping process (Peralta *et al.*, 2008). The relative contributions of these four processes to dorsal closure have been quantified based on a biophysical model, which was applied successfully to wild-type embryos and to laser and/or genetically perturbed embryos (Hutson *et al.*, 2003; Peralta *et al.*, 2007; Rodriguez-Diaz *et al.*, 2008; Toyama *et al.*, 2008). The kinematics of dorsal closure has been simulated with various force laws that characterize these biological processes (Layton *et al.*, 2009; Almeida *et al.*, 2011; Wang *et al.*, 2012). More recently, a nonequilibrium thermodynamic model has distinguished the contributions of tissue mechanics and adhesion dynamics to the overall zipping process (Lu *et al.*, 2015).

Apoptotic amnioserosa cells play an essential role in amnioserosa and zipping dynamics during dorsal closure (Toyama *et al.*, 2008; Muliyil *et al.*, 2011). About one-third of the force produced by the amnioserosa in wild-type embryos is due to apoptosis. This apoptotic force "turbocharges" the rate of native dorsal closure, tunes the asymmetric zipping rates during native closure, and is a sensitive mechanism for up-regulation of biomechanical processes to make closure robust.

Tissue-scale amnioserosa force production typically has been attributed in part to intracellular actomyosin force production that is then transmitted by intercellular adherens junctions (e.g., Sokolow *et al.*, 2012). Laser perturbation experiments confirm that the amnioserosa is under tension (Kiehart *et al.*, 2000; Hutson *et al.*, 2003; Franke *et al.*, 2005), as is the intracellular actomyosin cytoskeleton (Ma *et al.*, 2009). Furthermore, the magnitude of the amnioserosa force can be up-regulated in response to laser (Peralta *et al.*, 2007) and genetic (Toyama *et al.*, 2008) perturbations, presumably by up-regulation of cytoskeletal force production. It has been proposed that intracellular pressure modulates the magnitude of intercellular force transmission (Saias *et al.*, 2015).

Dorsal closure is an inherently 3D process. First, the surface of the embryo is curved, including the dorsal surface. More specifically, a vitelline membrane that underlies an external chorion helps shape the *Drosophila* embryo. The epidermis, separated from the vitelline by a fluid-filled perivitelline space, exhibits a curved ventral surface and a flatter (but not strictly flat) dorsal surface (Figure 1A). Experimentally, the surface curvature of the domed amnioserosa is asymmetric, with distinct line curvatures in the anteroposterior (A–P) and left-right (L–R) directions, and is evident in both light microscope (Kiehart *et al.*, 2000; Hutson *et al.*, 2003; Peralta *et al.*, 2007; Toyama *et al.*, 2008; Chen *et al.*, 2014; Saias *et al.*, 2015) and electron microscope (Turner and Mahowald, 1977; Underwood *et al.*, 1980; Eltsov *et al.*, 2015) studies. Second, zipping is a 3D process. Apposing leading-edge cells first come together at their apical ends and then square off basally to form a lateral junction (Lu *et al.*, 2015), where filopodia mediate the initial contact, and the seam includes overlapping single lamella (Eltsov *et al.*, 2015). Third, amnioserosa cells move inward during three classes of ingression processes, that is, processes by which amnioserosa cells internalize below the remaining amnioserosa tissue and undergo apoptosis (Kiehart *et al.*, 2000; Peralta *et al.*, 2007; Toyama *et al.*, 2008; reviewed in Sokolow *et al.*, 2012). One class of ingression characterizes ~10% of the amnioserosa cells throughout the dorsal opening during the mid-to-late stages of dorsal closure. Amnioserosa cells also ingress near the canthi as part of the zipping process and move underneath the seam. In addition,

amnioserosa cells ingress near the leading edges of the lateral epidermis. In some investigations, a slight compression during mounting was used to flatten the dorsal surface of the embryo and the amnioserosa (e.g., Kiehart *et al.*, 2000; Hutson *et al.*, 2003; Peralta *et al.*, 2007; Toyama *et al.*, 2008). In addition, confocal *z*-stacks frequently have been projected in the *z*-direction onto a "dorsal plane" (e.g., Sokolow *et al.*, 2012). Whether flattened into a plane during mounting or projected onto a plane during data analysis, in effect both approaches treat dorsal closure as an approximately two-dimensional (2D) process.

Here we report our quantitative investigation of dorsal closure in 3D, moving beyond the previous 2D treatments. We imaged live embryos labeled with fluorescent molecules with confocal microscopy. We segmented the time series of confocal images and analyzed them with Laplace's formula to investigate how tissue elastic properties help to shape the dorsal surface.

RESULTS AND DISCUSSION

Purse-string curvature and the dynamics of the amnioserosa/leading-edge junctions

There were two key ways that the purse strings deviated from a plane during the early-to-mid stages of dorsal closure. The curvatures are summarized in Figure 1D and Supplemental Movie S2, which present dorsal, sagittal, and transverse views of a GFP-moe-ABD embryo at a comparable stage of development to that shown in Figure 1C, and are quantified in Supplemental Movies S3 and S4. The *x*-direction is parallel to the A–P axis, the *y*-direction is parallel to the L–R axis, and the *z*-direction is perpendicular to the *xy*-plane. During early closure, each purse string tends to follow the curved surface of the embryo in the L–R direction (compare Figure 1, A and D, to visualize the 3D situation). The asterisk in the sagittal image of Figure 1D indicates the maximum dorsal opening in the L–R direction, where each purse string increasingly bowed over the lateral side of the embryo as it approached the maximal dorsal opening. Second, near each canthus, the purse strings were bent in the *z*-direction toward the embryo interior (*arrows*, sagittal and transverse images, Figure 1D). This deflection accounts for the larger range in the *z*-direction for the sagittal section relative to the transverse section in Figure 1C, where the dashed line in the sagittal section lies in a dorsal plane and passes through each seam. In other words, the sagittal section reports the total height of the dome, in contrast to the transverse section, which reports the height of the dome at the maximum dorsal opening. Supplemental Movies S3 and S4 detail the curvature changes throughout each purse string as closure progresses, which indicates that there are time-dependent 3D forces acting along each purse string.

The amnioserosa/leading-edge junction was increasingly indented by the purse strings as closure progressed (Figure 2). This increase is highlighted by comparing the left and right junctions at representative early and late stages, as shown in Figure 2, A and B, respectively, which are tracings of confocal images. Figure 2C, top, presents the stage dependence of the angles $\theta_{AS,L}$ and $\theta_{AS,R}$ defined by the apical surface of the amnioserosa (AS) as it approached the left (L) or right (R) leading edge, respectively. In Figures 2 and 3, the embryos were staged by the area of the dorsal opening. Zero degrees indicates the reference axis (horizontal dashed lines in Figure 2, A and B) in the L–R direction. A positive value for an angle corresponds to rotating above the reference axis and a negative value to rotating below it. Figure 2C indicates that the trend was for $\theta_{AS,L}$ and $\theta_{AS,R}$ (squares) to be largest at the earlier stages and to decrease as closure progressed. Figure 2C, bottom, presents the angles $\theta_{LE,L}$ and $\theta_{LE,R}$ (circles), which are the angles between either leading-edge cell (LE) and their respective reference axis as they approached the left or right leading edge (positive angles correspond to rotating above the reference axis). At the earlier stages, $\theta_{LE,L}$ and $\theta_{LE,R}$ have negative values (an arbitrary sign convention) and essentially tracked the curvature of the lateral epidermis (Figure 2A) as each purse string moved toward the dorsal midline (see next paragraph). However, with time, $\theta_{LE,L}$ and $\theta_{LE,R}$ became positive as the embryo surface increasingly indented at the two leading edge/amnioserosa junctions (Figure 2B).

The purse strings moved systematically as closure progressed, initially moving dorsally and then reversing to move in the ventral direction. Figure 2D reports the stage

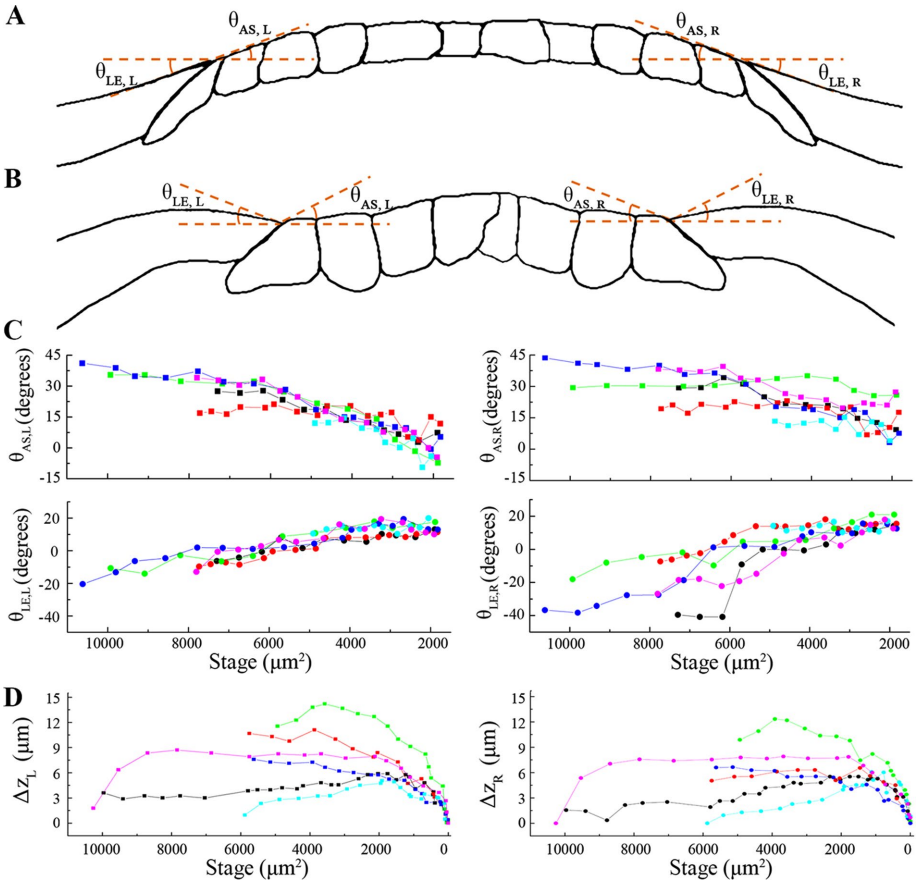

FIGURE 2: Indenting the leading edge/amnioserosa interfaces. (A, B) Traces of confocal images identify the angles between left and right (dashed horizontal) reference axes and the leading edges of the lateral epidermis ($\theta_{LE,L}$ and $\theta_{LE,R}$) or the amnioserosa ($\theta_{AS,L}$ and $\theta_{AS,R}$) during early (A) and mid (B) stages of closure. (C) Stage dependence of $\theta_{AS,L}$ (left, ■) and $\theta_{LE,L}$ (•) and $\theta_{AS,R}$ (right, ■) and $\theta_{LE,R}$ (•) for six embryos (distinguished by color). (D) Stage dependence of Δz_L and Δz_R at the maximum dorsal opening.

dependence of the displacements Δz_L and Δz_R, where the zero value for displacement corresponded to the final position of the purse string. The trend was for each purse string to follow the curved embryo surface (in the L–R direction) during the early stages of closure (larger displacements) and then increasingly indent the dorsal surface during the later stages (smaller displacements).

The curvature of the purse strings and the indentation of the dorsal surface raise questions about the forces acting along each purse string. Purse-string tension is the largest force associated with the dorsal closure's system of force-producing processes (Hutson *et al.*, 2003; Peralta *et al.*, 2007). More specifically, the amnioserosa is about two-thirds as stiff as the lateral epidermis, and a purse string is >10 stiffer than either the amnioserosa or the lateral epidermis. Consequently either tissue will be more susceptible than a purse string to bulge outward due to pressure internal to the embryo (discussed in the next section). Furthermore, previously we proposed that the deflection of the purse strings near each canthus is the consequence of an additional force localized to a canthus (Lu *et al.*, 2015). The ends of the purse strings begin to disassemble as apposing leading-edge cells zip (Lu *et al.*, 2015), which is consistent with the softening of purse-string ends to more readily accommodate these localized bends (see the three arrows in Figure 1D). Purse-string disassembly and the softening of purse string ends may support the formation of filopodia and lamellipodia and the junctional remodeling of apposing leading-edge cells during zipping (Jacinto *et al.*, 2002a; Eltsov *et al.*, 2015).

Amnioserosa curvature and dynamics

During the early-to-mid stages of dorsal closure, the amnioserosa was asymmetrically domed and bulged into the perivitelline space, where the purse strings and canthi border the dorsal opening. Figure 1C presents dorsal, sagittal, and transverse views of amnioserosa cell boundaries as determined by adherens junctions labeled with GFP–DE-cadherin. It highlights the difference in the curvatures for the A–P (*x*-axis) and L–R (*y*-axis) directions. At this stage of dorsal closure, the height of the dome was 20 ± 2 µm (see sagittal view), the canthus-to-canthus distance was 168 ± 2 µm, and the maximum dorsal opening in the L–R direction was 66 ± 2 µm (SDs determined by span of junction fluorescence). The asymmetry of the dome reflects the geometry of the dorsal opening, that is, the canthus-to-canthus arc was ~173 µm, and the arc in the L–R direction was ~70 µm, where the two arcs intersect at the top of the dome.

As closure progressed, the stage dependence of the domed amnioserosa exhibited two interesting phases. Initially, the dorsal opening closed along the curved surface of the embryo. The peripheral-most amnioserosa cells and the two purse strings moved dorsally (in the *y*- and *z*-directions). This is evident in the first four frames of Supplemental Movie S1 and the first six frames of Supplemental Movie S2. Subsequently the surface indented, and the amnioserosa moved toward the embryo interior as closure progressed.

The amnioserosa dome was smoothly and asymmetrically curved ($\kappa_{L-R} > \kappa_{A-P}$; Figure 3, A and C, and Supplemental Movie S5). κ_{A-P} and κ_{L-R} are the two principal curvatures at the top of the dome and are inversely related to the radii R_{A-P} and R_{L-R} (Figure 3C), respectively. The stage-dependent values for κ_{A-P}, κ_{L-R}, and the ratio $\kappa_{L-R}/\kappa_{A-P}$ are presented in Figure 3D. $\kappa_{L-R,avg}$ (20.0 ± 4.3 mm^{-1}) was greater than $\kappa_{A-P,avg}$ (3.7 ± 2.5 mm^{-1}; $N = 6$), which is consistent with the asymmetry of the dorsal opening. The sum of κ_{A-P} and κ_{L-R} was constant within experimental uncertainty until the later stages, when the area of the dorsal opening was ~3000 μm^2, as presented in Figure 3E, where $\Delta P/\alpha_{AS}$ is equal to $\kappa_{A-P} + \kappa_{L-R}$, as will be discussed later.

We first fitted the curvature of the amnioserosa dome with an asymmetric, 3D version of Laplace's formula (Defay *et al.*, 1966):

$$\Delta P = \alpha_{AS}(\kappa_{A-P} + \kappa_{L-R}) \quad (1)$$

where ΔP is the hydrostatic pressure difference across the amnioserosa and α_{AS} is the surface tension coefficient. In other words, if the pressure of the yolk exceeds that of the perivitelline space, the result is a net pressure outward (ΔP). The residuals in Figure 3B are the difference between the fit to the amnioserosa dome and the segmented DE-cadherin belts. The average residual was ~0.9 µm (at most ~1.2 µm) for each time slice during the early-to-mid stages for all of the embryos, which compares favorably to the spatial extent of the network of DE-cadherin belts (~2 µm wide, ~3 µm deep) and indicates that the curved amnioserosa is well fitted by Laplace's formula. Equation 1 indicates that the sum of the perpendicular contributions $\alpha_{AS}\kappa_{A-P}$ and $\alpha_{AS}\kappa_{L-R}$ balances ΔP, with this property applying to each location throughout the amnioserosa. Multiplying both sides of Eq. 1 by Δa, which is the cross-sectional area of an amnioserosa cell, recasts it as a force balance between the pressure term, $\Delta P \Delta a$, and the elasticity term, $\alpha_{AS}(\kappa_{A-P} + \kappa_{L-R})\Delta a$.

The value of $\Delta P/\alpha_{AS}$ essentially was constant from early-through-mid stages of closure, with an average value of 26 ± 7 mm^{-1} ($N = 6$; uncertainty due to biological variability). Figure 3E presents the stage dependence of the ratio $\Delta P/\alpha_{AS}$ for six embryos. Numerical uncertainties increased as the size of the dorsal opening decreased during the later stages (<3000 μm^2), obscuring any significant changes in $\Delta P/\alpha_{AS}$.

Next we investigated whether α_{AS} varied with location on the amnioserosa dome at any time slice. Assuming ΔP is constant throughout the amnioserosa, we fitted the data with two generalizations of Laplace's formula for a nonuniform surface tension coefficient. First, we investigated whether the surface tension coefficient was anisotropic, that is, whether the value along the A–P direction ($\alpha_{AS,A-P}$) differs from that along the L–R direction ($\alpha_{AS,L-R}$). Laplace's formula then takes the form

$$\Delta P = \alpha_{AS,\,A-P}\kappa_{A-P} + \alpha_{AS,\,L-R}\kappa_{L-R} \quad (2)$$

The resulting values for $\alpha_{AS,A-P}$ and $\alpha_{AS,L-R}$ agreed within ~3% (less than numerical uncertainty; $N = 6$). This result is consistent with an isotropic elastic epithelium. Then we investigated whether the surface tension coefficient in the anterior half of the dorsal opening ($\sigma_{AS,Ant}$) differed from that of the posterior half ($\sigma_{AS,Post}$). Previously we reported a greater prevalence of apoptosis in the anterior two-thirds of the dorsal opening during the mid-to-late stages of dorsal closure (Toyama *et al.*, 2008). Although there may be a trend ($\sigma_{AS,Ant}/\sigma_{AS,Post} = 1.18$; $p = 0.43$; $N = 6$), due to statistical uncertainty, we cannot conclude that $\sigma_{AS,Ant}$ differs from $\sigma_{AS,Post}$. In addition, we found no evidence in the residuals for any relatively "flat patches" that would correspond to apoptotic rosettes in the amnioserosa. We cannot rule out the possibility, however, that the apoptotic force may increase α_{AS} during mid-to-late stages of closure, which also would promote flattening of the amnioserosa. In any event, the asymmetric dome of the amnioserosa was well described by Eq. 1 during the early-to-mid stages of closure.

This analysis of the time dependence of the fitting parameter $\Delta P/\alpha_{AS}$ provides insight into the mechanical properties of the amnioserosa. The ratio of $\Delta P/\alpha_{AS}$ essentially was constant (within experimental uncertainty) from the early-to-mid stages of dorsal closure. Although it is possible that ΔP and α_{AS} vary as a function of time in a compensatory manner to maintain a constant ratio throughout the amnioserosa, it seems unlikely. If we assume that both ΔP and

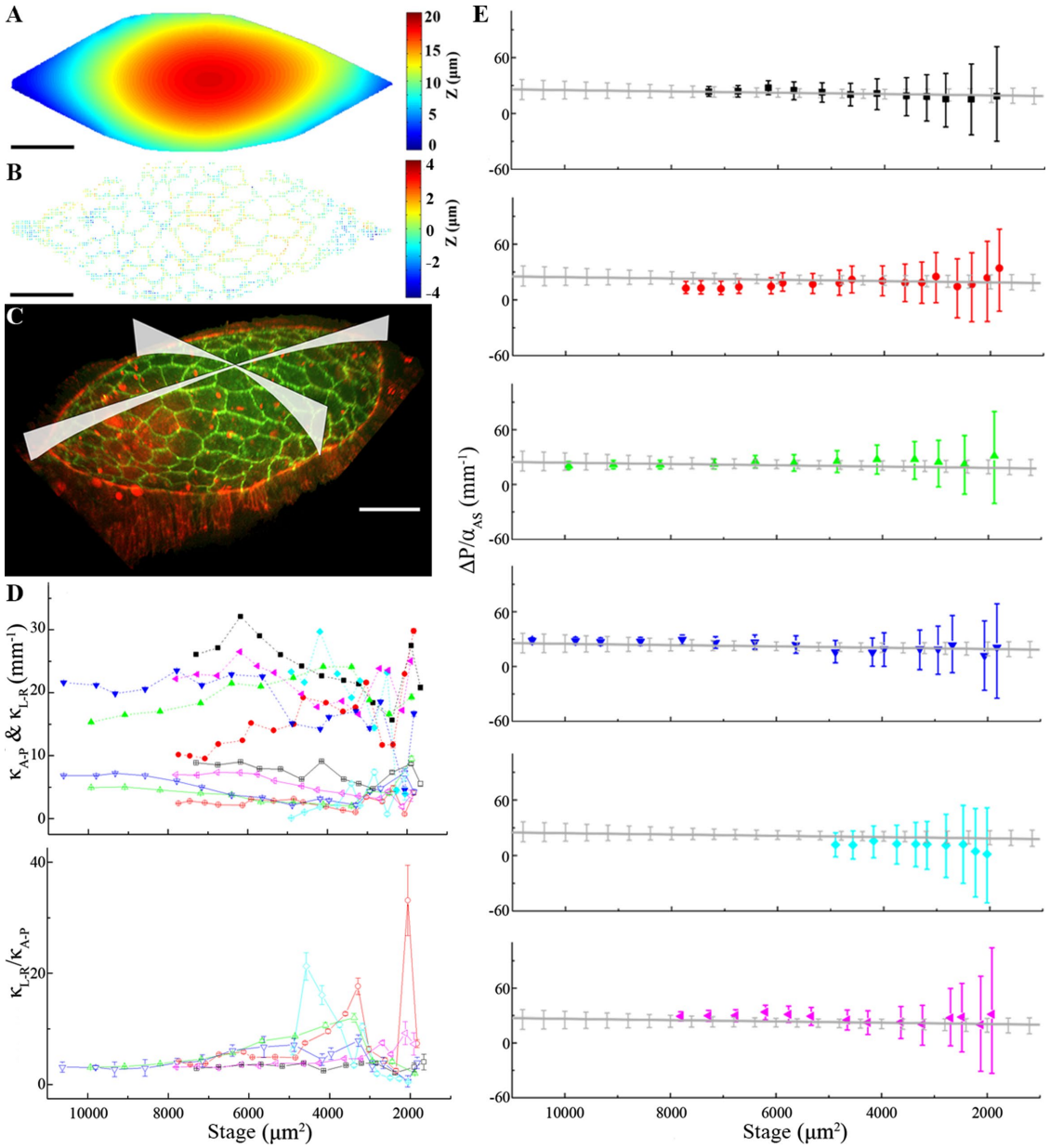

FIGURE 3: Amnioserosa dome. (A) Heat map of the height z of the amnioserosa, as determined by fitting the segmented image of an early-stage GFP–DE-cadherin embryo with Laplace's formula (image corresponds to the first symbol in the top data trace [black] of E). Anterior is to the right. Bar, 30 μm (A–C). (B) Heat map of residuals corresponding to A. (C) A 3D rendering of early closure for a GFP–DE-cadherin (green) and RFP-moe-ABD (red) embryo. Two orthogonal planes (white) that mark the curvature in the A–P and L–R directions are superposed on the confocal image and are intended as guides. (D) Plot of κ_{A-P} (open symbols) and κ_{L-R} (filled symbols) and a plot of the ratio $\kappa_{L-R}/\kappa_{A-P}$ during closure. (E) Stage dependence of $\Delta P/\alpha_{AS}$ for six embryos (distinguished by color). Average results for the six embryos are shown in gray.

α_{AS} are independently constant throughout the amnioserosa with little if any variability from the early-to-mid stages of closure, we can make the following observations. Although it may not be surprising that the internal pressure is constant throughout the dorsal opening at any one time, it is interesting that this pressure is nearly constant during the early-to-mid stages of closure. The doming of the amnioserosa is due to both ΔP and the fact that the amnioserosa is more compliant than (not as stiff as) the lateral epidermis or, to a greater extent, the purse strings. We interpret the internal overpressure as being exerted on the amnioserosa. This interpretation is supported by three observations. 1) It is standard protocol to dehydrate an embryo in preparation for microinjection to prevent extrusion of the cytoplasm due to the internal overpressure as seen in fully hydrated embryos (Van Deusen, 1976; Spradling and Rubin, 1982). 2) After laser dissection of amnioserosa, the tissue retracts to expose a substantial region of the amnioserosa-free dorsal opening without blowout (Kiehart *et al.*, 2000; Hutson *et al.*, 2003; Peralta *et al.*, 2007; Toyama *et al.*, 2008). 3) If the laser is focused too deeply, blowout occurs (Kiehart *et al.*, 2006; Lu *et al.*, 2015).

The amnioserosa dome is remarkably smooth during the early-to-mid stages of closure (the average residual was less than the spatial extent of DE-cadherin belts), and (within experimental uncertainties),

α_{AS} is isotropic and uniform throughout this tissue. The smooth, curved amnioserosa extended throughout the dorsal opening, anchored at the periphery of the dorsal opening by the two curved purse strings that are localized near the two leading edges of the lateral epidermis. These observations are consistent with the view that the surface tension coefficient α_{AS} is effectively time-averaged and any cell-to-cell variation in force production would drive oscillations in the shape of their apical cross-sections as measured by the fluorescence of the subapical DE-cadherin network throughout the amnioserosa (Sokolow *et al.*, 2012). Incidentally, it has been proposed that external pressure contributes to a mechanochemical mechanism for the oscillating basal surfaces of follicle cells in the expanding *Drosophila* egg chamber (Korida *et al.*, 2014). Here we have shown that the pressure internal to the embryo and the elastic properties of the amnioserosa, the lateral epidermis, and the purse strings contribute to shaping the dorsal surface. The amnioserosa pulls the two flanks of lateral epidermis together; however, since α_{AS} is isotropic, we attribute the asymmetric shape of the dorsal opening as being due to anisotropic elastic properties of the lateral epidermis.

MATERIALS AND METHODS

Overview of experimental approach

We imaged *z*-stacks of living embryos with fluorescently labeled proteins, including GFP-moe-ABD, which labels the F-actin cytoskeleton; GFP–DE-cadherin, which labels belts of subapical adherens junctions; and GFP–DE-cadherin/RFP-moe-ABD. The time series of confocal images were segmented to resolve the amnioserosa cells and the two purse strings in 3D. The two purse strings and the amnioserosa were quantified with Laplace's formula to analyze the elastic properties of the amnioserosa, the lateral epidermis, and the purse strings.

Fly stocks

We observed living embryos with either GFP- or GFP- and RFP-fusion transgenic stocks that were crossed into appropriate wild-type background based on standard genetic protocols (Greenspan, 2004). The transgenic, otherwise wild-type strain of *Drosophila* was homozygous for sGMCA-3.1 (flies included the genotype *w*/*w* or *w*/*Y*; *P*[*sqh*::*GFP*::*moe*,w^+]), a construct that encoded GFP fused to the F-actin binding region of moesin (GFP-moe-ABD), which was expressed under the control of the *spaghetti squash* promoter (Kiehart *et al.*, 2000) and used to visualize the F-actin cytoskeleton. To improve contrast at cell boundaries at the level of subapical adherens junctions, GFP–DE-cadherin driven by a ubiquitin promoter/enhancer cassette was expressed (Oda and Tsukita, 2001). To visualize simultaneously subapical junctional belts and actin cytoskeleton, we collected embryos from male and female parents of the genotype *w*; *e22c-Gal4*, *UAS-RFP-moe*, *ubi-DE-Cadherin-GFP*/*SM6a* (Brand and Perrimon, 1993). These embryos expressed GFP fused to DE-cadherin and RFP fused to the actin-binding domain of moesin (Singh and Kiehart, unpublished results,), primarily in the epidermis.

Embryo preparation and microscopy

Small population cages of well-maintained adult flies with appropriate genotypes were collected from 2-h egg lays. The embryos were then aged 22–24 h at 16°C to generate robust populations of dorsal-closure-staged embryos (Kiehart *et al.*, 2006). Subsequently the embryos were dechorionated and mounted in a modified halocarbon oil-immersion chamber between a gas-permeable membrane (Teflon) and a glass coverslip that allowed development to proceed while in vivo fluorescent imaging was performed (Kiehart *et al.*, 1994). Fluorescent images were collected from the early stages of closure (before the onset of canthus formation) and continued for 3–4 h at 23°C until closure was completed. All of the embryos completed dorsal closure and hatched.

Single-channel data (GFP–DE-cadherin or GFP-moe-ABD embryos) were acquired with a Zeiss LSM410 (488-nm excitation; Carl Zeiss, Minneapolis, MN) laser-scanning confocal microscope using a 63×, 1.4 numerical aperture (NA) oil-immersion objective. Scanning time was 2 s, and two raster scans were averaged to produce an image. A *Z*-scan contained 30–40 z-slices (in 0.6-µm steps) and required 150–200 s. Two-channel data (GFP–DE-cadherin, RFP-moe-ABD embryos) were acquired with a spinning-disk confocal system (Yokagawa CS-10) attached to a Zeiss Axio Imager.M2m microscope using a 40×, 0.9 NA dipping lens or a 40×, 0.9 NA multi-immersion objective. The exposure time in the green channel was 200 ms and in the red channel was 500 ms (the GFP construct fluoresced more intensely than the RFP construct). Similarly, *Z*-scans included either ~25–30 *z*-slices (in 1.0-µm steps, 40× dipping lens and 40× multi-immersion lens). The *Z*-scans were taken every 60 s. Sequences of images were stored for subsequent analyses, including 3D visualization with Imaris. We imaged 10 GFP–DE-cadherin embryos, 10 GFP-moe-ABD embryos, and 7 GFP–DE-cadherin and RFP-moe-ABD embryos. Four of the 10 GFP-*DE*-cadherin and 4 of the 10 GFP-moe-ABD embryos were compressed in mounting or the embryo was rotated such that the dorsal surface was no longer imaged: thus these embryos were not included in curvature calculations. Flattened embryos were used to compare the rates of closure ($N = 3$ for GFP-*DE*-cadherin, $N = 4$ for GFP-moe-ABD) to that of unflattened embryos ($N = 6$) and were statistically equivalent ($p = 0.35$).

Image segmentation

The goal of segmentation was to distinguish the fluorescence emitted by either the amnioserosa cell junctions (described in this paragraph) or the purse strings (described in the next paragraph) from background fluorescence. A custom segmentation algorithm was developed using MATLAB (MathWorks, Natick, MA) to determine the apical cross-sections in three dimensions of a substantial fraction of the amnioserosa cells during dorsal closure. The *x*-direction is parallel to the A–P axis, the *y*-direction is parallel to the L–R axis, and the *z*-direction is perpendicular to the *xy*-plane. The first part of the algorithm established an intensity threshold to exclude background fluorescence as well as fluorescence from both leading edge cells and the cells of the lateral epidermis. In practice, this compromised the segmentation of the peripheral-most amnioserosa cells that extended underneath each leading edge. Second, a masking step (in the *z*-direction) excluded endogenous yolk fluorescence. This step tracked the GFP–DE-cadherin fluorescence for the curved amnioserosa tissue and identified a range of local *z*-values (for each *x*, *y*) that bracketed the fluorescent edges of the amnioserosa cells. The GFP–DE-cadherin extended ~2 µm in the *xy*-plane and ~3 µm in the *z*-direction, as reported previously (Lu *et al.*, 2015). These first two parts of the algorithm were based on the previous mask-projection algorithm developed in our group (Sokolow *et al.*, 2012), which bounded the network of fluorescent edges in three dimensions. The third part of the algorithm quantified the *z*-value corresponding to the maximum fluorescence intensity within each range of local *z*-values, which was necessary for subsequent analyses. To do so required two numerical steps, since the fluorescence from a subapical belt of DE-cadherin was ~3 µm thick in the *z*-direction, and each voxel was $0.4 \times 0.4 \times 0.6$ µm^3 (40×, 0.9 NA objective). The first step (of the third part of the

segmentation algorithm) projected the 3D network of DE-cadherin fluorescence into the $z = 0$ plane, that is, determining the x_i, y_i values of the network. Here i is an index that enumerated each of the projected (into the $z = 0$ plane) fluorescent voxels (x_i, y_i, 0) that correspond to DE-cadherin. The second step quantified the brightest fluorescent spots along the ~3-μm-thick belts in the z-direction. More specifically, it searched through those voxels (x_i, y_i, z_i) that are stacked above a voxel (x_i, y_i, 0) (previously identified by the projection step) to quantify the brightest value z_i. Thus the second step converted the bounded stack of voxels specified by (x_i, y_i, 0) into a single voxel (x_i, y_i, z_i). Repeating this second step for all values of the index i restored the location information in the z-direction and completed the 3D segmentation process.

The purse strings were segmented in ImageJ (http://rsb.info.nih.gov/ij/) and MATLAB. Initially, the active contour algorithm (Kass *et al.*, 1987), implemented in ImageJ, was used to project the florescent intensity into the $z = 0$ plane to determine those pixels (x_i, y_i) that correspond to the two purse strings. Then the MATLAB algorithm (described in the preceding paragraph) quantified the z_i-values corresponding to the maximum florescence intensities throughout each purse string and restored the location information in the z-direction. This two-step process segmented the two purse strings, which were each quantified as a space curve in three dimensions (Pressley, 2010).

Laplace's formula and quantifying curvatures

Laplace's formula in three dimensions is well suited to modeling the elastic properties of the amnioserosa. Laplace's formula typically is introduced by modeling an elastic interfacial film, which produces a surface tension when stretched, separated by two fluids at different pressures (Nelson, 2004). Consequently mechanical equilibrium is characterized by a curved and stretched film. However, Laplace's formula is not limited to interfacial films and also applies to the deflection of a thin elastic plate into a dome (Landau and Lifshitz, 1986), that is, it also applies to amnioserosa constrained at its periphery by the two leading edges.

Laplace's formula can also be generalized for asymmetric deformations (e.g., Defay *et al.*, 1966). For the asymmetric amnioserosa dome, Laplace's formula has the form

$$\Delta P = \alpha_{AS}\left(\frac{1}{R_1}+\frac{1}{R_2}\right) \tag{3}$$

The direction of the vector $\Delta \boldsymbol{P}$ is perpendicular to the surface, where its magnitude $\Delta P = P_2 - P_1$ is the pressure difference across the surface. In our application, P_1 corresponds to the pressure of the perivitelline space, and P_2 corresponds to the internal pressure of the embryo. R_1 and R_2 are the principal radii of curvature at a given point on the surface, which varies with position. α_{AS} is the surface tension coefficient of the amnioserosa. For the special case of a spherical surface, $R_1 = R_2 = R$, and Eq. 3 reduces to the more familiar form for Laplace's formula (Nelson, 2004)

$$\Delta P = \frac{2\alpha}{R} \tag{4}$$

At the top of the dome (Figure 3C), the principal curvatures are given by $\kappa_{A-P} = 1/R_{A-P}$ and $\kappa_{L-R} = 1/R_{L-R}$. However, this result is not limited to the top of the dome, as the sum $\kappa_1 + \kappa_2 = \Delta P/\alpha_{AS}$ at each location of the dome (Defay *et al.*, 1966). Thus, for our application, Laplace's formula takes the form

$$\Delta P = \alpha_{AS}(\kappa_{A-P} + \kappa_{L-R}) \tag{5}$$

Under the condition of a slightly curved dome, Eq. 5 can be written in the form (Landau and Lifshitz, 1987)

$$\frac{\Delta P}{\alpha_{AS}} = -\left(\frac{\partial^2 z}{\partial x^2}+\frac{\partial^2 z}{\partial y^2}\right) \tag{6}$$

Inspection of Eq. 6 reveals the 3D character of Laplace's formula, in which each curvature κ_{A-P} and κ_{L-R} can be calculated by a second partial derivative of z with respect to either x or y, respectively.

We used Eq. 6 to fit each frame of the time series of the segmented confocal images of GFP–DE-cadherin fluorescence due to the amnioserosa using a successive overrelaxation method (Berman and Plemmons, 1994) implemented in MATLAB, resulting in polynomial expressions for the perpendicular line curvatures from which κ_{A-P} and κ_{L-R} were determined. The algorithm constrained the periphery of the amnioserosa to match the two purse strings. For the results reported in Figure 3E, initially the algorithm used a constant value for $\Delta P/\alpha_{AS}$ throughout the amnioserosa dome for each image, and the value of that constant was allowed to vary from image to image. Thus the curvature values were determined by fitting Laplace's formula to successive segmented confocal images (Figure 3D). To assess the quality of the fit, we compared the fitted values (x_i, y_i, $z_{i,fit}$) to the segmented values (x_i, y_i, z_i), where the average residual is given by

$$\frac{\sum_{i=1}^{N}\left|z_{i,fit} - z_i\right|}{N} \tag{7}$$

Here N is the total number of segmented points. For each time slice, the average residual was ~0.9 μm (at most ~1.2 μm), which compared favorably to the spatial extent of the network of DE-cadherin belts (~2 μm wide, ~3 μm deep). As the area of the opening decreased, the doming became progressively harder to resolve due to the diminishing extent of the amnioserosa (Figure 1B; dorsal, sagittal, and transverse views). More specifically, the uncertainties in κ_{A-P} and κ_{L-R} (staged at 4900 μm^2) ranged from 0.2 to 4.9% for six GFP–DE-cadherin embryos during relatively early stages of closure (Figure 3D). The increase in uncertainty when averaging during these early stages was due to biological variability and not numerical uncertainty. However, during relatively later stages, the uncertainty increased to 23 and 68% (time averages), respectively, when the area of the dorsal opening decreased from 4900 to 1800 μm^2.

We followed the stage-dependent indentation by quantifying the transverse interface between a leading edge cell and its neighboring, peripheral-most amnioserosa cell near the maximum dorsal opening. A reference axis (in the L–R direction) was placed in the dorsal plane such that it intersected the purse string of each leading edge (Figure 2A). The angle of this reference axis varied by no more than 1° from the early-to-mid stages of dorsal closure. MATLAB was used to calculate the angle between the reference axis and the apical surface of each leading edge. The calculation of the angle between the reference axis and the apical surface of the amnioserosa at the interface was based on the fitting of Eq. 6 to the segmented data.

ACKNOWLEDGMENTS

This research was supported by National Institutes of Health Grant GM033830.

REFERENCES

Almeida L, Bagnerini P, Habbal A, Noselli S, Serman F (2011). A mathematical model for dorsal closure. J Theor Biol 268, 105–119.

Attrill H, Falls K, Goodman JL, Millburn GH, Antonazzo G, Rey AJ, Marygold SJ, FlyBase Consortium (2016). FlyBase: establishing a Gene Group resource for *Drosophila melanogaster*. Nucleic Acids Res 44, D786–D792.

Berman A, Plemmons RJ (1994). Nonnegative Matrices in the Mathematical Sciences, Philadelphia: Society for Industrial Mathematics, 172–180.

Brand AH, Perrimon N (1993). Targeted gene expression as a means of altering cell fates and generating dominant phenotypes. Development 191, 103–117.

Chen BC, Legant WR, Wang K, Shao L, Milkie DE, Davidson MW, Janetopoulos C, Wu XS, Hammer JA III, Liu Z, *et al*. (2014). Lattice light-sheet microscopy: imaging molecules to embryos at high spatiotemporal resolution. Science 346, 1257998.

David JV, Tishkina A, Harris JC (2010). The PAR complex regulates pulsed actomyosin contractions during amnioserosa apical constriction in *Drosophila*. Development 137, 1645–1655.

Defay R, Prigogine I, Bellemans A, Everett DH (1966). Surface Tension and Adsorption, New York: John Wiley and Sons, 6–10.

Eltsov M, Dube N, Yui Z, Pasakarnis L, Haselmann-Weiss U, Brunner D, Frangakis AS (2015). Quantitative analysis of cytoskeletal reorganization during epithelial tissue sealing by large-volume electron tomography. Nat Cell Biol 17, 605–614.

Foe VE, Alberts BM (1983). Studies of nuclear and cytoplasmic behavior during the five mitotic cycles that precede gastrulation in *Drosophila* embryogenesis. J Cell Sci 61, 31–70.

Franke JD, Montague RA, Kiehart DP (2005). Nonmuscle myosin II generates forces that transmit tension and drive contraction in multiple tissues during dorsal closure. Curr Biol 15, 2208–2221.

Greenspan RJ (2004). Fly Pushing: The Theory and Practice of *Drosophila* Genetics, 2nd ed., Cold Spring Harbor, NY: Cold Spring Harbor Laboratory Press.

Harden N (2002). Signaling pathways directing the movement and fusion of epithelial sheets: lessons from dorsal closure in *Drosophila*. Differentiation 70, 181–203.

Hutson MS, Tokutake Y, Chang MS, Bloor JW, Venakides S, Kiehart DP, Edwards GS (2003). Forces for morphogenesis investigated with laser microsurgery and quantitative modeling. Science 300, 145–149.

Jacinto A, Wood W, Balayo T, Turmaine M, Martinez Arias A, Martin P (2000). Dynamic actin-based epithelial adhesion and cell matching during *Drosophila* dorsal closure. Curr Biol 10, 1420–1426.

Jacinto A, Wood W, Woolner S, Hiley C, Turner L, Wilson C, Martinez-Arias A, Martin P (2002a). Dynamic analysis of actin cable function during Drosophila dorsal closure. Curr Biol 12, 1245–1450.

Jacinto A, Woolner S, Martin P (2002b). Dynamic analysis of dorsal closure in *Drosophila*: from genetics to cell biology. Dev Cell 3, 9–19.

Jankovics F, Brunner D (2006). Transiently reorganized microtubules are essential for zippering during dorsal closure in *Drosophila melanogaster*. Dev Cell 11, 375–385.

Kaltschmidt JA, Lawrence N, Morel V, Balayo T, Fernández BG, Pelissier A, Jacinto A, Arias AM (2002). Planar polarity and actin dynamics in the epidermis of *Drosophila*. Nat Cell Biol 4, 937–944.

Kass M, Witkin A, Terzopoulos D (1987). Snakes: active contour models. Int J Comput. Vis 1, 321–331.

Keller R, Davidson LA, Shook DR (2003). How we are shaped: the biomechanics of gastrulation. Differentiation 71, 171–205.

Kiehart DP, Galbraith CG, Edwards KA, Rickoll WL, Montague RA (2000). Multiple forces contribute to cell sheet morphogenesis for dorsal closure in *Drosophila*. J Cell Biol 149, 471–490.

Kiehart DP, Montague RA, Rickoll AL, Foard D, Thomas GH (1994). Methods in Cell Biology, ed. LSB Goldstein and EA Fyrerg, San Diego, CA: Academic Press.

Kiehart DP, Tokutake Y, Chang MS, Hutson MS, Wiemann J, Peralta XG, Toyama Y, Wells AR, Rodriguez A, Edwards GS (2006). Ultraviolet laser microbeam for dissection of *Drosophila* embryos. In: Cell Biology: A Laboratory Handbook, Vol. 3, 3rd ed., ed. JE Celis, San Diego, CA: Elsevier, 87–103.

Korida S, He L, Xiong LP, Lan G, Montell DJ, Sun SX (2014). Mechanochemical regulation of oscillatory follicle cell dynamics in the developing *Drosophila* egg chamber. Mol Biol Cell 25, 3709–3716.

Landau LD, Lifshitz EM (1986). Theory of Elasticity, 3rd ed., Oxford, UK: Reed Educational and Professional Publishing, 50–53.

Landau LD, Lifshitz EM (1987). Fluid Mechanics, 2nd ed., Elmsford, NY: Pergamon Press, 238–250.

Layton AT, Toyama Y, Yang GQ, Edwards GS, Kiehart DP, Venakides S (2009). *Drosophila* morphogenesis: tissue force laws and the modeling of dorsal closure. HFSP J 3, 441–460.

Lu H, Sokolow A, Kiehart DP, Edwards GS (2015). Remodeling tissue interfaces and the thermodynamics of zipping during dorsal closure in *Drosophila*. Biophys J 109, 2406–2417.

Ma X, Lynch HE, Scully PC, Hutson MS (2009). Probing embryonic tissue mechanics with laser hole drilling. Phys Biol 6, 036004.

Mateus AM, Martinez Arias A (2011). Patterned cell adhesion associated with tissue deformations during dorsal closure in *Drosophila*. PLoS One 6, e27159.

Muliyil S, Krishnakumar P, Narasimha M (2011). Spatial, temporal and molecular hierarchies in the link between death, delamination and dorsal closure. Development 138, 3043–3504.

Narasimha M, Brown NH (2004). Novel functions for integrins in epithelial morphogenesis. Curr Biol 14, 381–385.

Nelson P (2004). Biological Physics: Energy, Information, Life, New York: W. H. Freeman.

Oda H, Tsukita S (2001). Real-time imaging of cell-cell adherens junctions reveals that *Drosophila* mesoderm invagination begins with two phases of apical constriction of cells. J Cell Sci 114, 493–501.

Peralta XG, Toyama Y, Hutson MS, Montague R, Venakides S, Kiehart DP, Edwards GS (2007). Upregulation of forces and morphogenic asymmetries in dorsal closure during *Drosophila* development. Biophys J 92, 2583–2596.

Peralta XG, Toyama Y, Kiehart DP, Edwards GS (2008). Emergent properties during dorsal closure in *Drosophila* morphogenesis. Phys Biol 5, 015004.

Pressley A (2010). Elementary Differential Geometry, 2nd ed., London: Springer-Verlag, 29–54.

Rodriguez-Diaz A, Toyama Y, Abravanel DL, Wiemann JM, Wells AR, Tulu US, Edwards GS, Kiehart DP (2008). Actomyosin purse strings: renewable resources that make morphogenesis robust and resilient. HFSP J 2, 220–237.

Saias L, Swoger J, D'Angelo A, Hayes P, Colombelli J, Sharpe J, Salbreaux G, Solon J (2015). Decrease in cell volume generates contractile forces driving dorsal closure. Dev Cell 33, 611–621.

Sokolow A, Toyama Y, Kiehart DP, Edwards GS (2012). Cell ingression and apical shape oscillations during dorsal closure in *Drosophila*. Biophy J 102, 969–979.

Spradling AC, Rubin GM (1982). Transposition of cloned P elements into *Drosophila* germ line chromosomes. Science 218, 341–347.

Toyama Y, Peralta XG, Wells AR, Kiehart DP, Edwards GS (2008). Apoptotic force and tissue dynamics during *Drosophila* embryogenesis. Science 321, 1683–1686.

Turner FR, Mahowald AP (1977). Scanning electron microscopy of *Drosophila melanogaster* embryogenesis. Dev Biol 57, 403–416.

Underwood EM, Turner FR, Hahowald AP (1980). Analysis of cell movements and fate mapping during early embryogenesis in *Drosophila melanogaster*. Dev Biol 74, 286–301.

Van Deusen EB (1976). Sex determination in germ line chimeras of *Drosophila melanogaster*. J Embryol Exp Morphol 37, 173–185.

Wang QM, Feng JJ, Pismen LM (2012). A cell-level biomechanical model of *Drosophila* dorsal closure. Biophys J 103, 2265–2274.